Engineering Structures 199 (2019) 109583

Contents lists available at ScienceDirect

Engineering Structures

journal homepage: www.elsevier.com/locate/engstruct

Seismic behavior and damage evolution for retrofitted RC frames using haunch viscoelastic damping braces

Yao-Rong Dong, Zhao-Dong Xu*, Qiang-Qiang Li, Ye-Shou Xu, Zheng-Han Chen

Key Laboratory of C&PC Structures of the Ministry of Education, Southeast University, Nanjing, China

ARTICLE INFO

Keywords:
Non-invasive retrofit
Haunch viscoelastic damping braces
Seismic behavior
Axial load ratio
Failure mode

ABSTRACT

To upgrade the existing RC frame structure system with insufficient seismic design and improve the seismic design of the RC frame structures, a novel and advanced frame structure system retrofitted by adding haunch viscoelastic damping braces (HVEDB) is presented in this study based on the good energy dissipation performance, the low-cost and non-invasive addition of viscoelastic dampers. For a comprehensive and systematic research of this new structure system, the seismic behavior of ten RC frames and another ten RC frames added by HVEDB with the axial load ratio (ALR) of 0.1–1.0 are carried out under horizontal sinusoidal steady-state excitation loading, including the hysteretic behavior, load-bearing capacity, stiffness degradation, energy dissipation capacity, additional damping ratio and rebar strain at key locations. On this basis, four reasonable damage indicators at the material scale are proposed, and a comparative study on the damage evolution about two types of frames at the material scale in the whole process is carried out. The study results show that the addition of HVEDB can greatly improve the seismic performance such as load-bearing capacity, lateral stiffness, deformation capability and energy dissipation, and it changes the failure mode of the RC frames. The HVEDB can provide the effective protection for the beam-column joints by transferring the damage region from the beam-column joint to the frame beam successfully, which guarantee the seismic design requirements of "strong nodes and weak components" avoiding the brittle failure mode of frame structure under high ALR.

1. Introduction

Reinforced concrete (RC) frame buildings have been widely constructed for commercial, industrial and multi-family residential use in seismic-prone regions in the world [1]. However, several earthquake damage investigations have found that RC frame structures were seriously damaged under earthquake excitation. The beam-column joint region was the most critical and weakest link in the frame structure system, because the damage and failure of the joint would lead to the serious degradation of lateral load-bearing capacity and even the overall collapse of the structure [2–4]. In the experimental study on the seismic performance of RC frame structures, especially for these frame structures that have only been designed for gravity loads without considering seismic loads in the past, it has been confirmed that the RC frame structure system was difficult to meet the expected inherent weakness of "strong nodes and weak members" in multiple post-earthquake observations [5–7].

Many researchers explored various strategies to upgrade the existing RC frame structure system with inadequate seismic design and improved the seismic design of RC frame structures. They provided sufficient protection for beam-column joint area to ensure the seismic safety of the frame structure. Some scholars have adopted thin RC jackets [8], ferrocement jackets with embedded diagonal reinforcements [9], steel and pure aluminium shear panels [10] as fuses, and they have used steel plate with anchor bolts or welded steel strip [11], steel prop and curb [12], diagonal metallic haunch system [13], buckling-restrained braces [14,15], single bracing system of shape memory alloy [16], hysteretic damped braces[17] for the retrofit and reinforcement of the RC frame structures. Experimental and numerical simulation studies have shown that these strategies were very effective in improving the seismic performance of beam-column joints in terms of strength, stiffness, deformability and the failure mode of the frame structure. Other scholars have proposed to retrofit and reinforce the RC frame structure by the use of high-performance materials, including fiber-reinforced polymer [18–22], carbon fiber reinforced polymers composites [23–25], glass fiber-reinforced polymer composites [18], basalt fiber reinforced polymer [26], prefabricated high-performance fiber-reinforced cementitious composite [27], strain hardening cementitious composite [19], steel fiber reinforced concrete [28], etc. Experimental and numerical simulation results have shown that the use

* Corresponding author.
E-mail addresses: yaorong099@163.com (Y.-R. Dong), zhdxu@163.com (Z.-D. Xu).

https://doi.org/10.1016/j.engstruct.2019.109583
Received 8 January 2019; Received in revised form 23 July 2019; Accepted 23 August 2019

of these high-performance materials can greatly improve the strength and ductility of the beam-column joints and the failure mode of the frame structures.

However, the issues on cost, invasiveness and practical implementation remained the most challenging aspects of retrofitting the RC frame structures with inadequate seismic design. The viscoelastic damper is simple in construction, low-cost, convenient in installation, easy in replacement and non-invasive, and it also has good energy dissipation performance with an advantage of addition stiffness [29–32]. In this paper, a new frame structure system retrofitted by using haunch viscoelastic damping braces is proposed. This novel structure system can guarantee the building area and headroom avoiding the impact on the buildings' use (function) to the utmost. Compared with the traditional retrofitting strategies, the haunch viscoelastic damping braces can greatly improve the energy dissipation efficiency of the structure.

To systematically study the seismic performance and failure mechanism of this new structure system, the seismic behavior of ten reinforced concrete frame structures (CFs) and another ten another ten RC frame structures with haunch viscoelastic damping braces (VFs) with the ALR of 0.1–1.0 are carried out under horizontal sinusoidal steady-state excitation loading, including the hysteretic behavior, load-bearing capacity, stiffness degradation, energy dissipation capacity, additional damping ratio and rebar strain at key locations. On this basis, several reasonable damage indicators at the material scale are proposed, and a comparative study on the damage evolution about two types of frame structures at the material scale in the whole process is carried out.

2. Numerical investigations on the seismic behavior of RC frames with HVEDB

2.1. Design of RC frames with HVEDB

There are ten CFs, which are identified as CF1 to CF10 respectively, and another ten VFs, which are identified as VF1 to VF10 respectively are designed for this study. The cross section of frame column with a height of 1000 mm has a length of 160 mm and a width of 160 mm. The cross section of frame beam with a span of 1840 mm has a width of 100 mm and a height of 200 mm. The rigid base beam has a length of 3390 mm, a width of 440 mm and a height of 400 mm. The other design parameters of VFs are the same as those of CFs except for the haunch viscoelastic damping braces (HVEDB). Fig. 1 illustrates the dimensions, construction and HVEDB layout details of VFs. This HVEDB has four layers for viscoelastic material, and the size of viscoelastic material layer is 200 mm long × 150 mm width × 10 mm thick. The thickness of the constrained steel plate is 10 mm. The HVEDB are set at 460 mm (L/4) from the beam end with an angle of 45°. One end of the HVEDB is hingedly connected to the beam, and the other end is hingedly connected to the column.

2.2. Numerical model and relevant material properties

The concrete damage plasticity (CDP) model is employed for the constitutive relationship of concrete materials. Defining the CDP model in ABAQUS requires the uniaxial tensile and compressive mechanical behaviors of the concrete materials. The uniaxial tensile and compressive load cycle with different stiffness is illustrated in Fig. 2(a), and their annotations are calculated according to reference [33], respectively

$$\sigma_c = (1 - d_c)E_0(\varepsilon_c - \varepsilon_c^{pl}) \quad (1)$$

$$\sigma_t = (1 - d_t)E_0(\varepsilon_t - \varepsilon_t^{pl}) \quad (2)$$

where, σ_c and σ_t are the compressive and tensile stresses of concrete respectively. E_0 is the initial elastic stiffness; d_c and d_t are damage

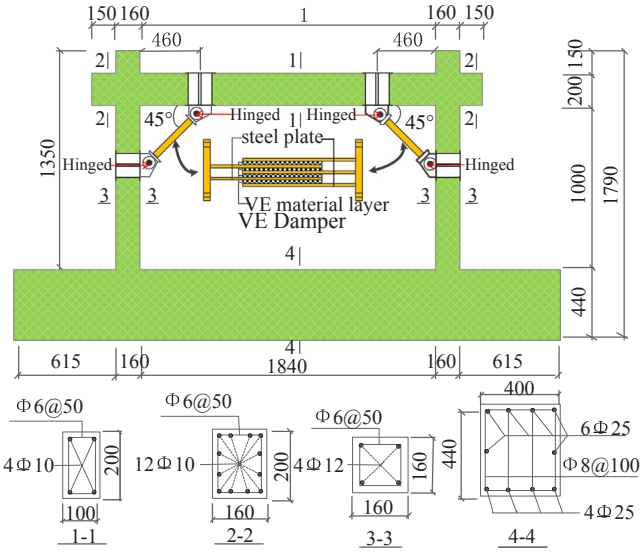

Fig. 1. Geometries and reinforcement details for RC frames with haunch viscoelastic damping braces (all dimensions in mm).

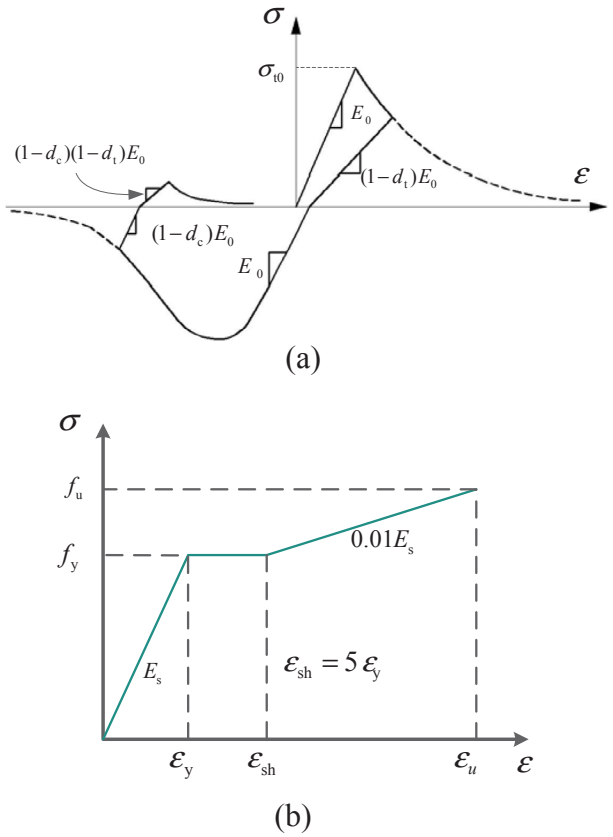

Fig. 2. Stress-strain relationship. (a) A single, uniaxial tensile-compressive loading cycle. (b) Stress-strain relationship of steel.

variables explained in detail in subsequent study; ε_c^{pl} and ε_t^{pl} are plastic strains for compression and tension respectively.

Two independent variables of d_t and d_c about uniaxial tensile and compressive damage are defined in the CDP model to consider the degradation response of concrete. The current code [34] explains the expression of the compressive damage coefficient. As follows:

$$d_t = \begin{cases} 1 - \rho_t[1.2 - 0.2x^5] & x \leqslant 1 \\ 1 - \frac{\rho_t}{\alpha_t(x-1)^{1.7}+x} & x > 1 \end{cases} \tag{3}$$

$$\rho_t = \frac{f_t}{E_c \varepsilon_{tu}} \tag{4}$$

$$x = \frac{\varepsilon_t}{\varepsilon_{tu}} \tag{5}$$

where, d_t is uniaxial tensile damage; α_t is the parameter value of uniaxial tensile stress-strain curve in the falling segment for the concrete. E_c is the elastic modulus of concrete. f_t is the representative value of uniaxial tensile strength for the concrete. ε_{tu} is the peak tensile strain corresponding to the representative value of uniaxial tensile strength for the concrete. ε_t is the uniaxial tensile strain for the concrete.

$$d_c = \begin{cases} 1 - \frac{\rho_c n}{n-1+x^n} & x \leqslant 1 \\ 1 - \frac{\rho_c}{\alpha_c(x-1)^2+x} & x > 1 \end{cases} \tag{6}$$

$$\rho_c = \frac{f_c}{E_c \varepsilon_{cu}} \tag{7}$$

$$n = \frac{E_c \varepsilon_{cu}}{E_c \varepsilon_{cu} - f_c} \tag{8}$$

$$x = \frac{\varepsilon_c}{\varepsilon_{cu}} \tag{9}$$

where d_c is uniaxial compressive damage. α_c is the parameter value of uniaxial compressive stress-strain curve in the falling segment for the concrete. f_c is the representative value of uniaxial compressive strength for the concrete. ε_{cu} is the peak compressive strain corresponding to the representative value of uniaxial compressive strength for the concrete. ε_c is the uniaxial compressive strain for the concrete.

As shown in Fig. 2(b), the tri-linear stress-strain mode [35] is employed for the constitutive relationship of the steel. The finite element model of frames adopts the separate method [33]. The 8-node linear brick (C3D8R) unit is used for concrete elements, while the 2-node linear 3-D truss (T3D2) unit is employed for rebar elements [33]. And the rebar is embedded into the concrete by the EMBED command. All degrees of freedom at the bottom of the confined base beam form the embedded end, and the bottom of the column is linked with the base beam by TIE. The SPRINGA and DASHPOTA units are adopted for simulating the haunch viscoelastic damping braces. The SPRINGA and DASHPOTA units have good convergence during very high deformation. The articulated connection at both ends of the truss is simulated by releasing the rotational degrees of freedom at both ends of the SPRINGA and DASHPOTA units. More detailed information can be found in the ABAQUS user's manual [33]. The mechanical model of the viscoelastic damper adopts the Equivalent fractional Kelvin model proposed by Xu [36] as given by Eq. (10), which can accurately describe the mechanical performance parameters of G_1, G_2 and η for viscoelastic dampers with the change of temperature and frequency.

$$\left.\begin{array}{c} G_1 = q_0 + q_1 \alpha_T^r \omega^r \cos(r\pi/2) \\ G_2 = q_1 \alpha_T^r \omega^r \sin(r\pi/2) \\ \eta = (q_1 \alpha_T^r \omega^r \sin(r\pi/2))/(q_0 + q_1 \alpha_T^r \omega^r \cos(r\pi/2)) \end{array}\right\} \tag{10}$$

where, q_0 and q_1 are the coefficients related to the viscoelastic materials. r is the order of fraction, α_T is the temperature transformation coefficient, ω is the frequency, G_1 is the storage modulus, G_2 is the loss modulus and η is the loss factor. The equivalent stiffness K_e and equivalent damping C_e of elastic damper can be obtained by the following equation.

$$K_e = n_v G_1 A_v / h_v \tag{11}$$

$$C_e = n_v \eta G_1 A_v / \omega h_v = \eta K_e / (2\pi f) \tag{12}$$

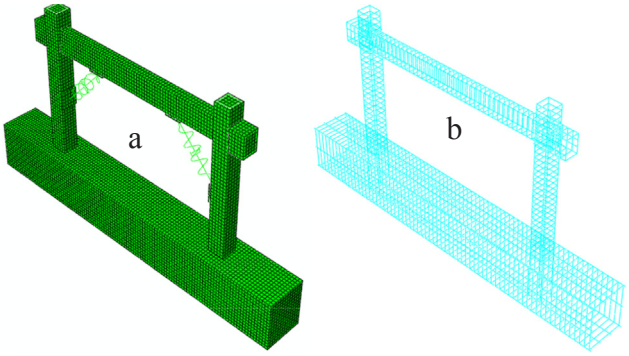

Fig. 3. Finite element models. (a) RC frames with haunch viscoelastic damping braces. (b) Reinforcement bars.

where, n_v is the number of viscoelastic material layers, A_v and h_v are the shear area and thickness of viscoelastic material layers respectively, and f is the loading frequency.

The viscoelastic damper with the same parameters and type developed by Xu [36] is employed for this research. The viscoelastic material has four layers with the sheared area of $A_v = 0.03\text{m}^2$ and the thickness of $h_v = 0.01\text{m}$. The temperature is taken to be 20 °C.

2.3. Load application and control

Fig. 3 demonstrates the nonlinear finite element model of the frames established by the above method. Table 1 lists the ALRs applied to the structure under different working conditions. Since the viscoelastic damper is a speed-dependent energy dissipating device, the dynamic loading method should be employed to reflect its real situation. Therefore, a horizontal excitation load of $u_d = u_0 \cdot \sin \omega t (\omega = 2\pi f, f = 1\text{Hz})$ is applied to the load control of displacement amplitude. Fig. 4 shows the increasing lateral displacement.

2.4. Verification of finite element model

Fig. 5 illustrates that the reinforced concrete frame specimens were tested in the test set up [37]. Fig. 1 shows the detailed information of reinforced concrete frames.

The finite element model of reinforced concrete frame specimen can be established according to the above finite element method. Fig. 6 shows a good agreement about the experimental and simulated force-displacement loops of reinforced concrete frame specimens. The load at the yield points of simulation and experiment is 67.19 kN and 63.69 kN and the error is 5.06%. The load at the peak points of simulation and experiment is 84.79 kN and 80.15 kN and the error is 5.47%. In a word, there is a good agreement between the finite element simulation and experimental results for the reinforced concrete frames.

Table 1
ALR and the applied axial.

Specimens	ALR ($N/f_c^{'}A_g$)	Axial load (kN)
CF1,VF1	0.1	80.9
CF 2,VF2	0.2	161.8
CF 3,VF3	0.3	242.7
CF 4,VF4	0.4	323.6
CF 5,VF5	0.5	404.5
CF 6,VF6	0.6	485.4
CF 7,VF7	0.7	566.3
CF 8,VF8	0.8	647.2
CF 9,VF9	0.9	728.1
CF 10,VF10	1.0	809.0

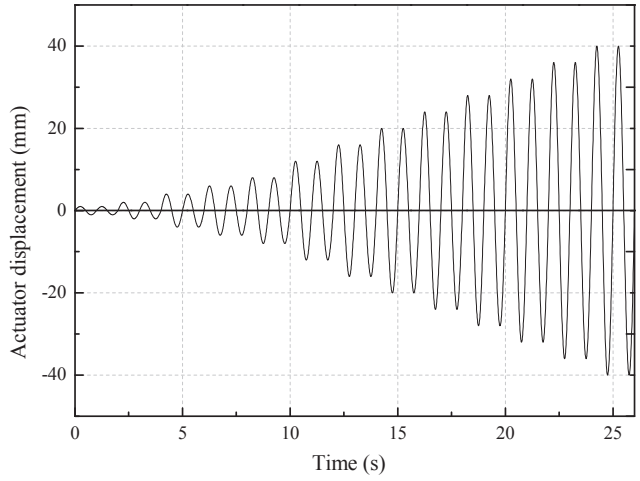

Fig. 4. The increasing lateral displacements.

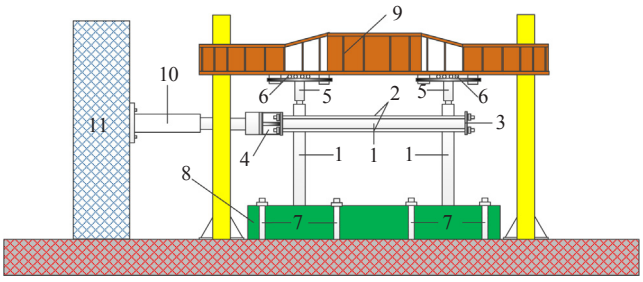

Fig. 5. Test setup for RC frames.

3. Effect of ALR on the seismic behavior

The ALR of the column is the main design parameter which affects the seismic performance of the frame structures. Many studies [38,39] have shown that, ALR has a significant effect on the cracking development, ductility performance and failure pattern of RC frames. ALR is defined by the equation of ALR = $N/f_c^{'}A_g$, where N, $f_c^{'}$ and A_g are axial load, concrete compression strength and cross section of column. For the RC frame structures with HVEDB, the controlled ALR of frame column is a major measure to prevent the collapse of the structures. Moreover, the seismic behavior of the frame column with the change of ALR would also affect the energy dissipation capacity of the HVEDB in the structure. The ALR of the frame column has a significant influence on the failure mode of the structure. Therefore, it is necessary to study the effect of ALR on the seismic behavior of VFs.

3.1. Load-displacement response

Fig. 7 illustrates a comparison of the hysteresis curves between the VFs and CFs. When the ALR is within 0.1–0.5, the bearing capacity and stiffness in the next cycle for both CFs and VFs are slightly lower than those in the previous cycle under the same level of displacement control. With the increasing ALR, the fullness degree of hysteresis curve about CFs reduces. The plumpness degree of hysteresis curve about VFs is almost constant, but the bearing capacity about VFs is significantly improved. The number of cycles that CFs can withstand and the ultimate deformation reduce gradually after crossing the peak load. When the ALR is within 0.6–1.0, the bearing capacity and stiffness in the next cycle for CFs are significantly lower than those in the previous cycle under the same level of displacement control. With the increase of ALR, the improvement of bearing capacity for both CFs and VFs almost stops. After passing the peak load for CFs, the stability of hysteresis curve significantly decreases, the hysteresis curve becomes obviously flat, the bearing capacity seriously attenuates, the ultimate deformation and the number of load cycles significantly reduce and the energy dissipation capacity rapidly reduces. After passing the peak load for VFs, the stability of hysteresis curve slightly decreases, the hysteresis curve is still full and the energy dissipation capacity keeps better. Under a certain drift, the hysteretic performance of VF suddenly falls. The reason is that the severe damage of VFs is concentrated at concrete in joint region, the column bottom and the beam with HVEDB. At the same time, the damage generation causes the reduced efficiency on the stiffness and damping provided by HVEDB.

In general, under each level of ALR, the hysteresis curve is relatively elongated and it has a slight pinch phenomenon for CFs. The energy dissipation of the structure mainly relies on the plastic deformation of frame beams and frame columns for CFs. The hysteresis curve is plumpness and the hysteresis loop presents a spindle shape for VFs. The hysteresis curve for VFs is obviously fuller than that for CFs. The area of hysteresis loop and bearing capacity for VFs are significantly larger than those for CFs. It indicates that the energy dissipation capacity and load-bearing capacity of the RC frame structure are significantly

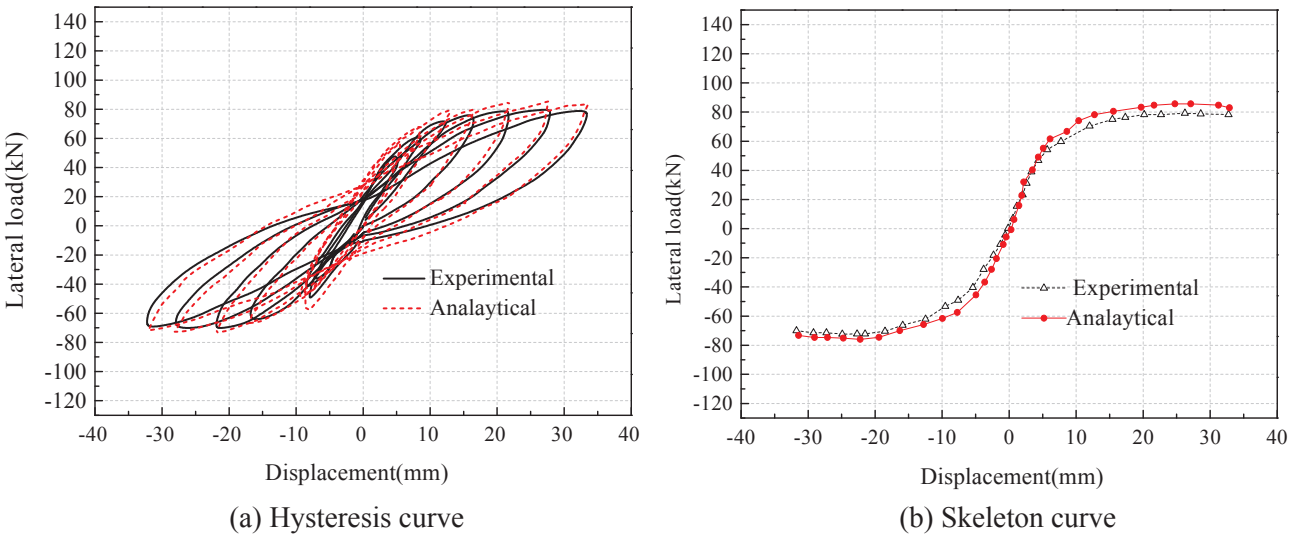

Fig. 6. Comparison of analytical and experimental load-displacement curve.

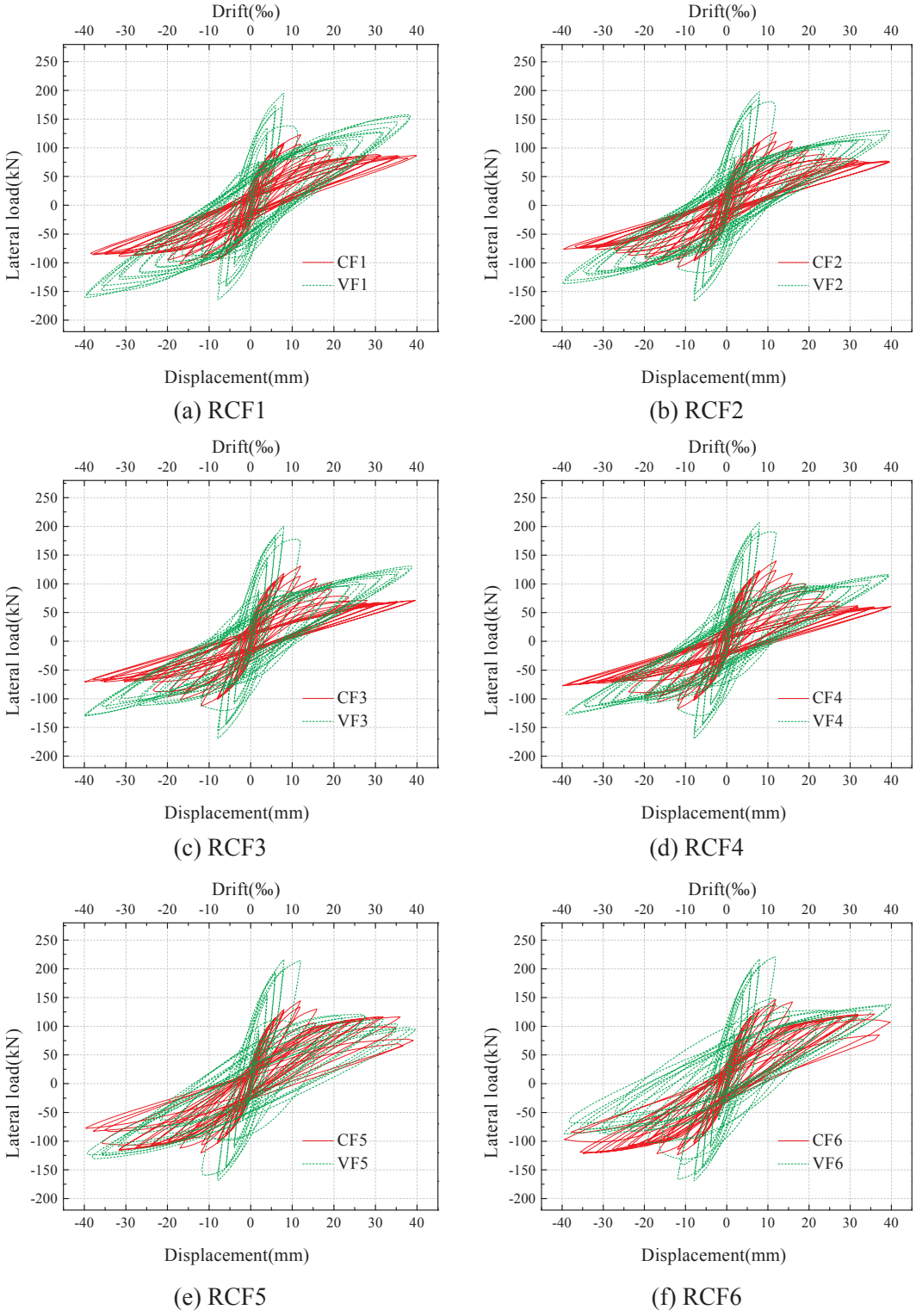

Fig. 7. Comparison of the hysteresis curves between the VFs and CFs.

improved by adding HVEDB.

3.2. Load-bearing capacity

The load-bearing capacity improvement coefficient is defined as the ratio of peak load for VF to the peak value of load-bearing capacity for CF. The load-bearing capacity degradation coefficient is defined as the ratio of the specific load-bearing capacity corresponding to the ultimate displacement to the peak value of load-bearing capacity, and it can reflect the ductility performance of the structure.

Fig. 8 demonstrates the comparison on the peak value of load-bearing capacity under various levels of ALR and the bearing capacity improvement coefficient with the change of ALR for CFs and VFs. The load-bearing capacity of VFs is greatly improved compared with CFs under each level of ALR. The load-bearing capacity of CFs and VFs both present a rising tendency with the increase of ALR, and the load-bearing

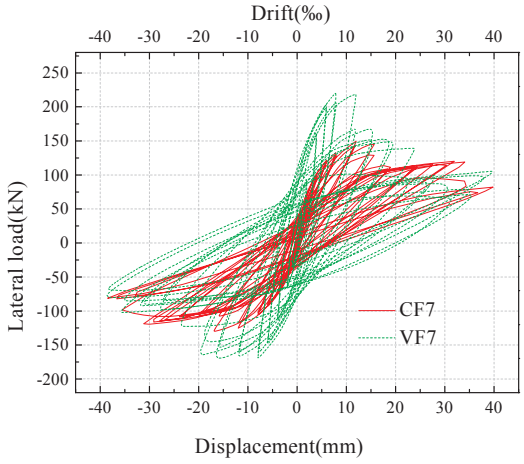

(g) RCF7

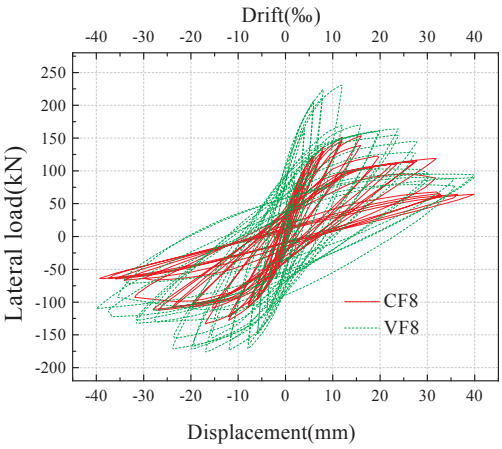

(h) RCF8

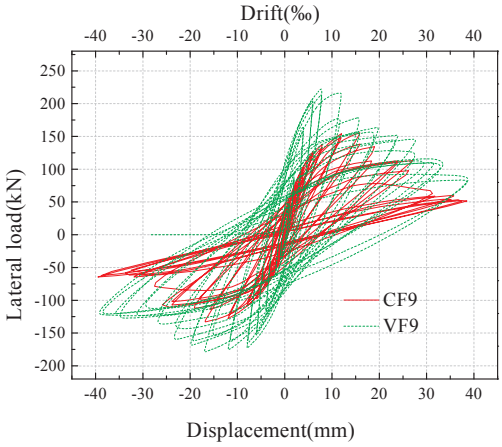

(i) RCF9

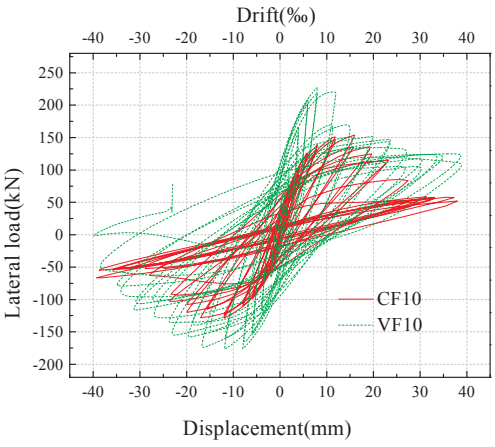

(j) RCF10

Fig. 7. (*continued*)

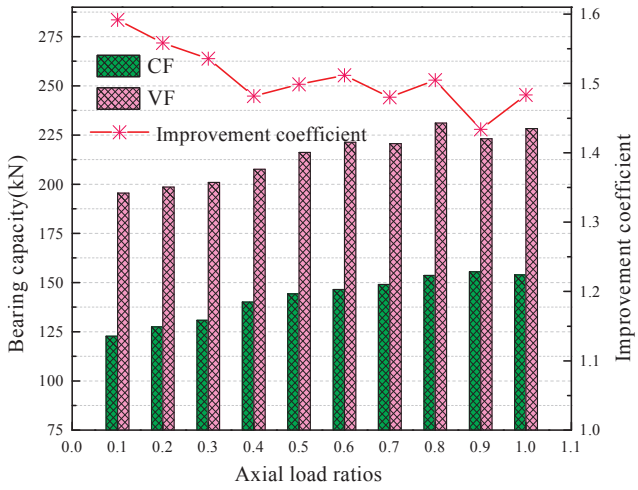

Fig. 8. Comparison load-bearing capacity and the improvement coefficient.

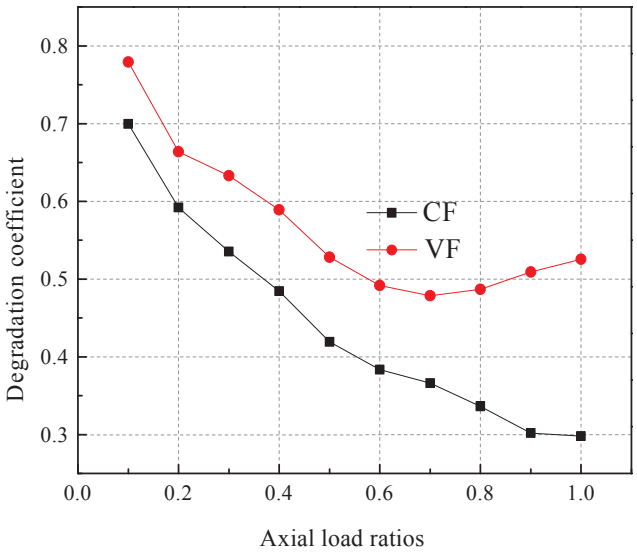

Fig. 9. Bearing capacity degradation coefficient curves.

capacity increases slowly even tends to stop under the condition of 0.1–0.5. When the ALR is within 0.1–0.5, the bearing capacity improvement coefficient gradually decreases with the increasing ALR. When the ALR is greater than or equal to 0.5, the bearing capacity improvement coefficient basically tends to be stable and it is between within 1.43–1.59. It shows that the bearing capacity improvement coefficient of the structure is less affected by the ALR. To ensure the design safety of the structure, the recommended bearing capacity improvement coefficient is taken as 1.43.

Fig. 9 demonstrates the bearing capacity degradation coefficient with the change of ALR for CFs and VFs. The bearing capacity degradation coefficient of CFs continuously reduces with the increase of ALR. When the ALR is within 0.1–0.5, the bearing capacity degradation coefficient of VFs gradually decreases with the increasing ALR. When the ALR is within 0.5–1.0, the bearing capacity degradation coefficient of VFs presents a rising trend. It can be seen from the comparison of the two curves that, the difference of the bearing capacity degradation coefficient for CFs and VFs gradually is magnified as the ALR increases, and the bearing capacity degradation coefficient for VFs is increased by 11.39%–76.47% compared with CFs. This shows that the energy-dissipating haunch braces have a significant effect on restraining the bearing capacity degradation of the structure, and the restriction effect is gradually enhanced as the ALR increases.

3.3. Stiffness

The stiffness degradation of the frames within different cyclic cycles can be measured by secant stiffness under the same displacement control point. The stiffness improvement coefficient is defined as the average value of the increased proportion about the stiffness of VF to CF under different displacement amplitude.

Fig. 10 illustrates the comparison on the stiffness degradation curves of CFs and VFs under each level of ALR. The stiffness degradation pattern of CF and VF follows a very similar pattern. With the increase of displacement amplitude, the secant stiffness of the forward and reverse loading for CFs and VFs both decrease. The secant stiffness greatly decreases at first, and it gradually becomes more moderate in the later. Under the same ALR and displacement amplitude, the secant stiffness of VFs is significantly larger than that of CFs.

Fig. 11 demonstrates the comparison on the initial stiffness under various levels of ALR and the stiffness improvement coefficient with the change of ALR for CFs and VFs. The initial stiffness of VFs is greatly improved compared with CFs at the same ALR. With the increasing ALR, the initial stiffness of CFs and VFs both gradually increase. When the ALR is within 0.1–0.5, the stiffness improvement coefficient is stable ranging from 39.20% to 42.33%, which indicates that the HVEDB produces a stable and superior effect in restricting the stiffness degradation of the structure with the change of ALR. When the ALR is within 0.5–1.0, the stiffness improvement coefficient increases gradually with the increasing ALR, and it can reach up to 63.35%. It indicates that the HVEDB enhances the better inhibition effect on the stiffness degradation of the structure as the ALR increases.

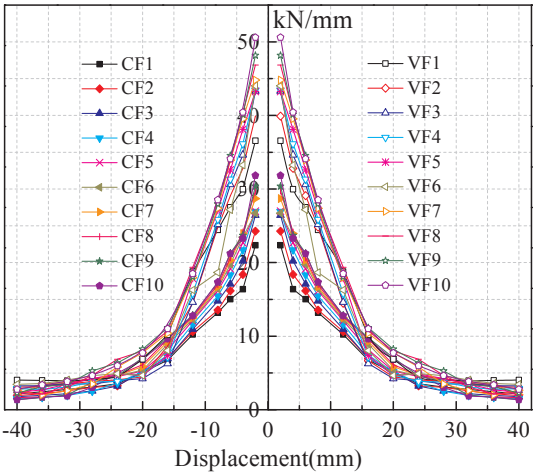

Fig. 10. Comparison on the stiffness degradation curve.

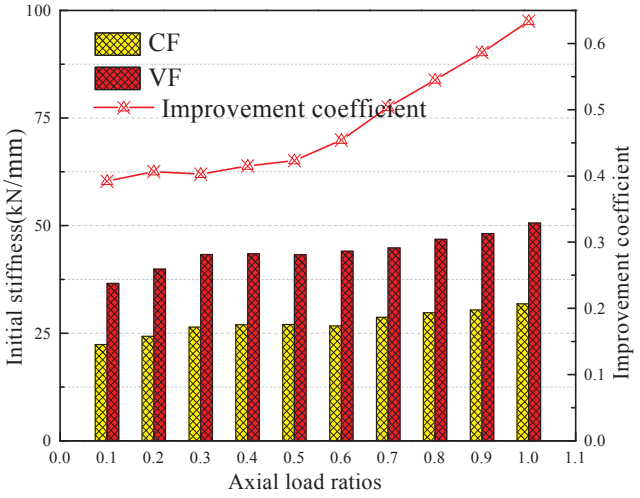

Fig. 11. Initial stiffness and the stiffness improvement coefficient curve.

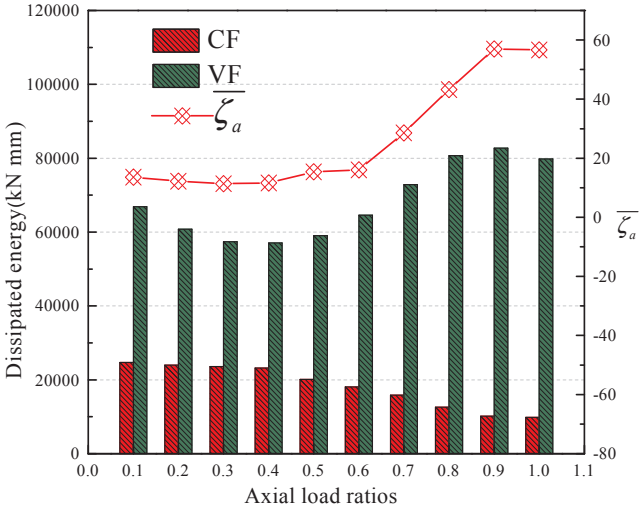

Fig. 12. The energy dissipation capacity and the average additional damping ratio $\bar{\zeta}_a$.

3.4. Energy dissipation capacity and additional damping ratio

Fig. 12 illustrates the comparison on the energy dissipation capacity of CFs and VFs under various levels of ALR and the average additional damping ratio (marked as $\bar{\zeta}_a$) of VFs with the change of ALR. When the ALR is in the range of 0.1–0.4, the energy dissipation capacity of CFs remains basically unchanged with the increase of ALR. The energy dissipation capacity of CFs gradually reduces when the ALR is larger than 0.4. When the ALR is in the range of 0.1–1.0, the energy dissipation capacity of VFs slightly reduces first and then gradually rises with the increase of ALR. And the energy dissipation capacity of VFs reaches a minimum under the ALR of 0.4. The energy dissipation capacity of VFs is significantly higher than that of CFs under the same ALR. When the ALR is in the range of 0.1–0.6, the average additional damping ratio of VFs remains basically stable, that is, $\bar{\zeta}_a$ is within 12.00%–16.07%. When the ALR is in the range of 0.6–1.0, the average additional damping ratio of VFs gradually increases with the increase of ALR, and $\bar{\zeta}_a$ can reach up to 56.96%.

Fig. 13 illustrates the energy dissipation capacity of HVEDB for VFs with the change of displacement amplitude under various levels of ALR. Under the small displacement amplitude of 0–8 mm, the energy dissipation of HVEDB gradually increases with the increase of displacement amplitude. And the ALR has a little influence on the energy

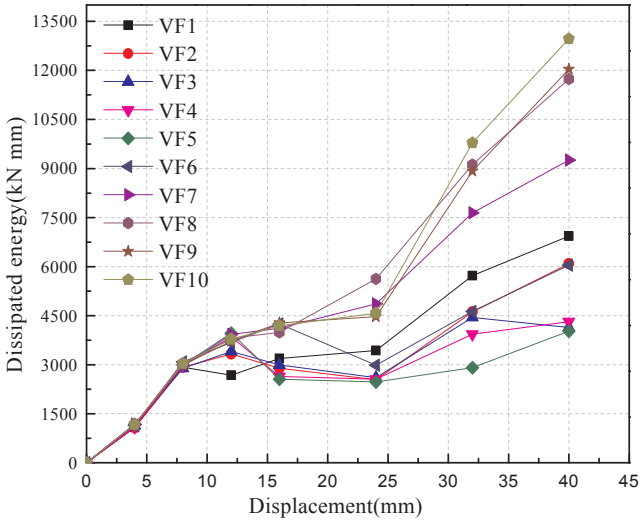

Fig. 13. Energy dissipation capacity of HVEDB.

dissipation of HVEDB. Under the medium displacement amplitude of 8–24 mm, the energy dissipation of HVEDB remains stable with the change of ALR. Under the large displacement amplitude of 24–40 mm, the energy dissipation of HVEDB slowly increases with the increase of displacement amplitude when the ALR is within 0.1–0.6, and the energy dissipation of HVEDB rapidly increases with the increase of displacement amplitude when the ALR is within 0.6–1.0.

Fig. 14 illustrates the area ratio (marked as ϕ) about the hysteresis loop between VFs and CFs and the ratio (marked as ψ) of the energy dissipation of HVEDB to the total energy dissipation of VFs with the change of ALR. The change trend of ϕ and ψ keeps basically consistent with the increase of ALR. When the ALR is in the range of 0.1–0.6, ϕ and ψ remain basically stable, that is, ϕ is within 2.43–3.01 and ψ is within 0.58–0.66. When the ALR is in the range of 0.6–1.0, ϕ and ψ both increase with the increase of ALR, even ϕ and ψ can reach up to 8.15 and 0.87 respectively.

In summary, when the ALR is under the condition of 0.1–0.6, the HVEDB for VFs can play a stable and superior role in terms of energy dissipation. When the ALR is under the condition of 0.6–1.0, the energy dissipation capacity of HVEDB for VFs is gradually enhanced with the increase of ALR and the HVEDB still plays an effective role in energy dissipating.

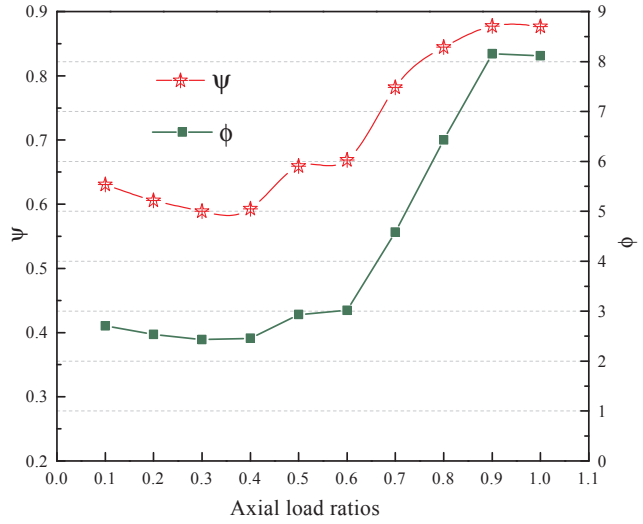

Fig. 14. ϕ and ψ curves.

3.5. Critical point strain analysis

Fig. 15 demonstrates the displacement-strain curves of reinforcement rebar at the beam-column joints of CFs and VFs under the action of excitation load. Due to the length limitation of the article, only these cases where the ALR is 0.1, 0.5 and 1.0 are listed. In the whole process of excitation load, the reinforcement strain of CFs and VFs grows with the increase of load amplitude. Under each level of ALR from 0.1 to 1.0, the reinforcement strain at the beam-column joints of VFs is much lower than that of CFs. And the stirrups and longitudinal reinforcement at the beam-column joints of VFs are in the elastic stage.

The reduction amplitude about the strain maximum of the stirrup for VFs relative to the CFs is marked as μ_1, and the reduction amplitude about the strain maximum of longitudinal reinforcement for VFs relative to the CFs is marked as μ_2. Fig. 16 illustrates the strain maximum of reinforcement rebar at the beam-column joints of CFs and the reduction amplitude of strain maximum with the change of ALR.

The strain maximum of the stirrup at the beam-column joints of CFs is larger than that of VFs under the same ALR. The stirrup strains at the beam-column joints of CFs and VFs are small values and the strain maximum of the stirrup varies little with the change of ALR, which indicates that the stirrup strain is insensitive to the change of ALR. The strain maximum of longitudinal reinforcement at the beam-column joints of CFs and VFs increases with the increasing ALR. The growth curve of strain maximum for CFs is steep, while the growth curve for VFs is gentle. The strain maximum of longitudinal reinforcement at the beam-column joints of VFs is much smaller than that of CFs under the same ALR. And the VF structure is still in the elastic deformation stage under the large ALR. The longitudinal reinforcement of CFs quickly enters the plasticity state under the large ALR, which indicates that the longitudinal reinforcement of CFs should be especially strengthened under the large ALR. The reduction amplitude about the strain maximum of the stirrup decreases with the increase of ALR, and μ_1 can reach up to 83.59%. The reduction amplitude about the strain maximum of longitudinal reinforcement presents a large fluctuation when the ALR is under the condition of 0.1–0.3. The reason is that the maximum strain of longitudinal reinforcement transitions from tensile strain to compressive strain. The reduction amplitude about the strain maximum of longitudinal reinforcement gradually increases with the increase of ALR when the ALR is under the condition of 0.3–1.0. The longitudinal reinforcement of VFs is still elastically deformed under the large ALR, and μ_2 can reach up to 88.09%.

In summary, the strain of the stirrup and longitudinal reinforcement at the beam-column joints of the frame structure significantly reduces after the HVEDB is added to the CFs. Under the displacement excitation of maximum amplitude, the strain of the stirrup and longitudinal reinforcement is still weak and within the elastic stage. Therefore, the HVEDB provides a good protection for the beam-column joint zone.

4. The damage evolution in the whole process

As we know, the compressive properties of concrete materials are far superior to tensile properties, and the concrete materials mainly provide the compressive bearing capacity when it is applied by the force. Generally, the tensile strength of concrete materials is not taken into account and the concrete materials are allowed to work with cracks in the seismic design of the structure. At the same time, each performance point of the frame structure corresponds to the inflection point of the compressive damage of the concrete materials. However, the tensile damage of concrete materials develops too quickly and presents a large dispersion, and the tensile damage of concrete materials is not sensitive to the performance change of the frame structure. Therefore, the compressive damage of concrete materials is selected as an evaluation index for the damage evolution analysis of the frame structure in this paper.

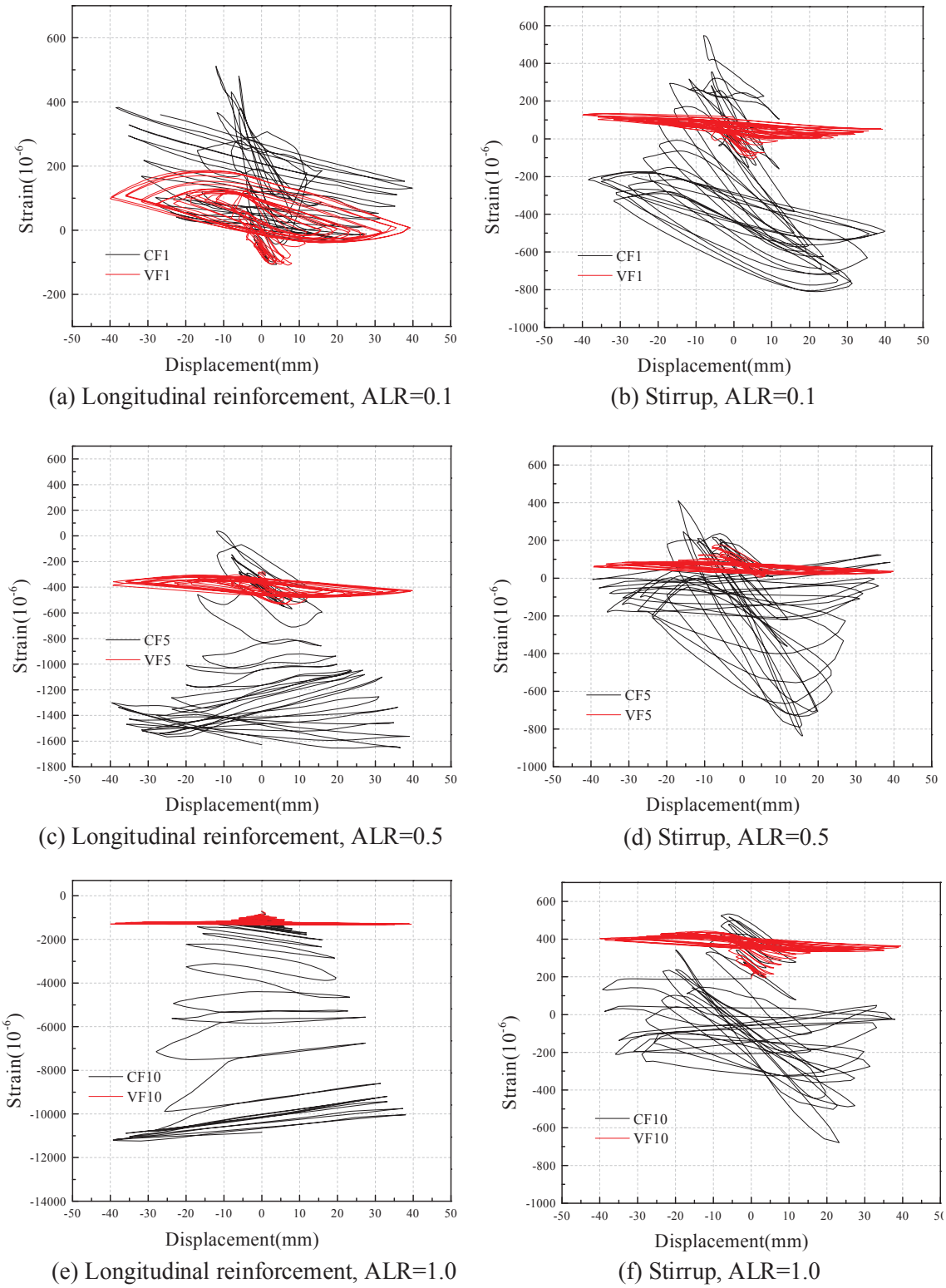

Fig. 15. Strain-displacement curves for reinforcement rebar at beam-column joints.

4.1. Comparison of each level of damage

Base on the Park-Ang damage theory at the component scale [40] and the results of finite element analysis, Fig. 17 illustrates the damage evolution of CFs and VFs in the whole process from basic intact to component failure. In the damage level of basically intact, there is no compressive damage occurring in the CFs and VFs and both of them are still within the elastic stage. In the damage level of slightly damaged, the minor compressive damage of CFs begins to appear at the edge of the column bottom, while the minor compressive damage of VFs begins to appear at the edge of the column bottom and beam bottom with HVEDB. In the damage level of moderately damaged, the compressive damage of CFs slowly expands and gradually accumulates at the column bottom, beam ends and beam-column joints, while the compressive

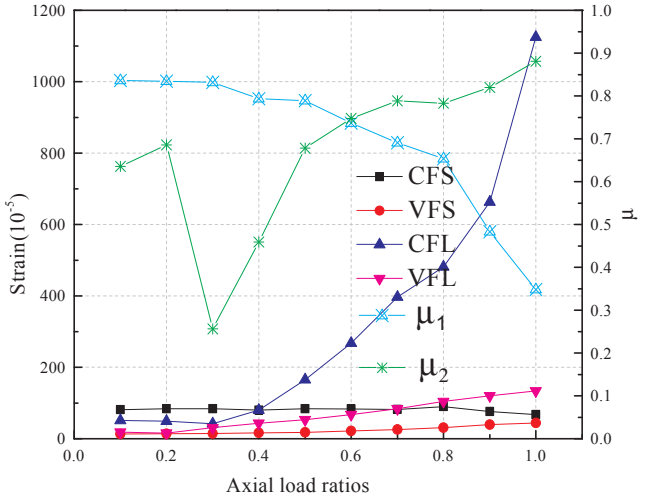

Fig. 16. Strain maximum of reinforcement rebar and reduction amplitude μ.

damage of VFs slowly expands and gradually accumulates at the column bottom and beam bottom with HVEDB. In the damage level of seriously damaged, the compressive damage at the column bottom of CFs simultaneously expands to the column top and column center, and the compressive damage at the beam-column joints of CFs rapidly expands and continuously accumulates. The compressive damage at the column bottom of VFs simultaneously expands to the column top and central axis and the compressive damage at the beam bottom with HVEDB quickly expands to the beam top and middle span. In the damage level of member failure, the compressive damage of CFs basically penetrates at the beam-column joints and column bottom, while the compressive damage of VFs basically penetrates at the column bottom and the beam with HVEDB.

The compressive damage of CFs is concentrated at the beam-column joints, the 0–1/3H of the column bottom and the beam ends, while the compressive damage of VFs is concentrated at the 0–1/3H of the column bottom and the beam with HVEDB. The above-mentioned locations about CFs and VFs where the compressive damage is concentrated at should be especially enhanced in the seismic design of the structure. The addition of HVEDB can provide the effective protection for the beam-column joints of frame structure by restraining the damage development at the beam-column joints, which realizes the ductile seismic design of “strong nodes and weak components”.

4.2. Selection of damage indicators

According to the damage development of CFs and VFs in five different stages listed in section 4.1, four damage indicators are selected to describe the damage evolution of CFs and VFs in the whole process from basic intact to component failure, as shown in Fig. 17.

The first, second, third and fourth damage indicator reflects the degree of compressive damage at the column bottom, the beam-column joints, the beam with HVEDB and the column with HVEDB of the frame structure, and they are expressed by D_c, D_j, D_b and D_z respectively. These four indicators can reflect the main characteristics of compressive damage development about CFs and VFs under different damage levels, which includes the damage degree of the frame structure, the damage range and distribution rule of frame columns, beam-column joints and frame beams.

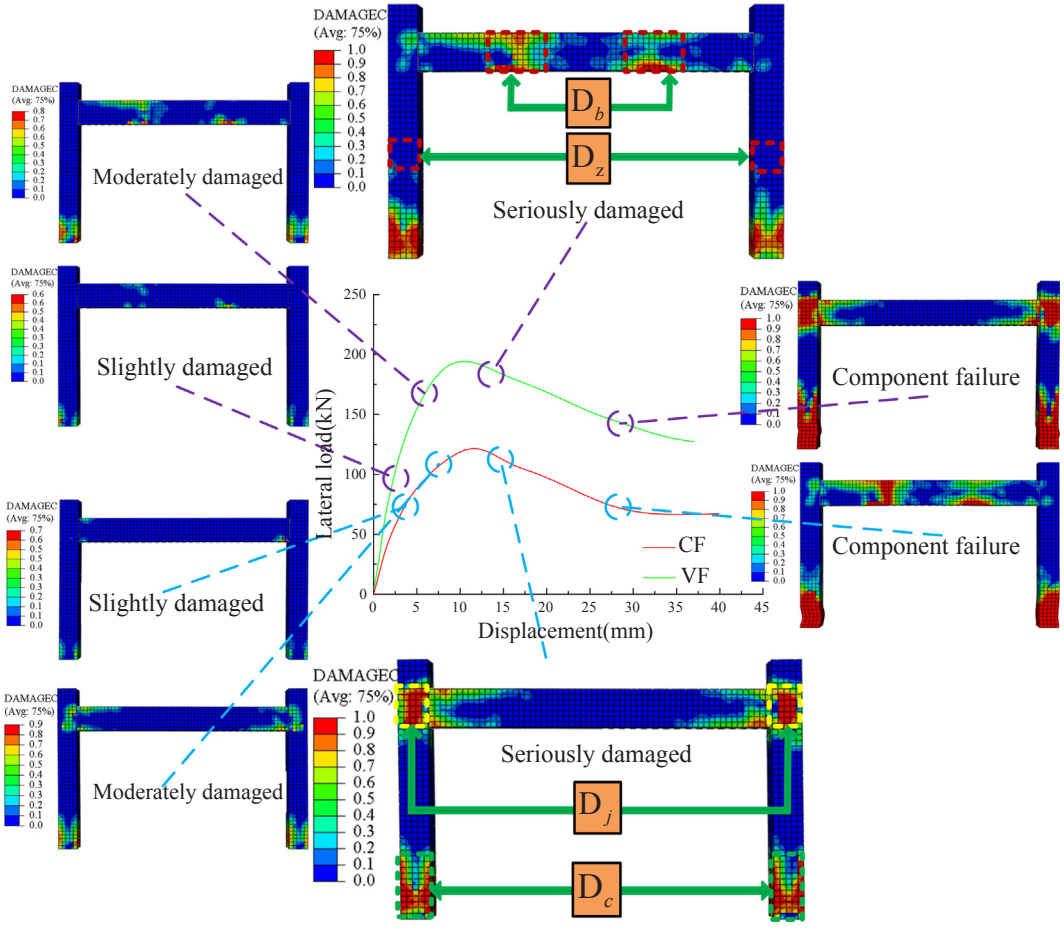

Fig. 17. The damage evolution of CFs and VFs in the whole process.

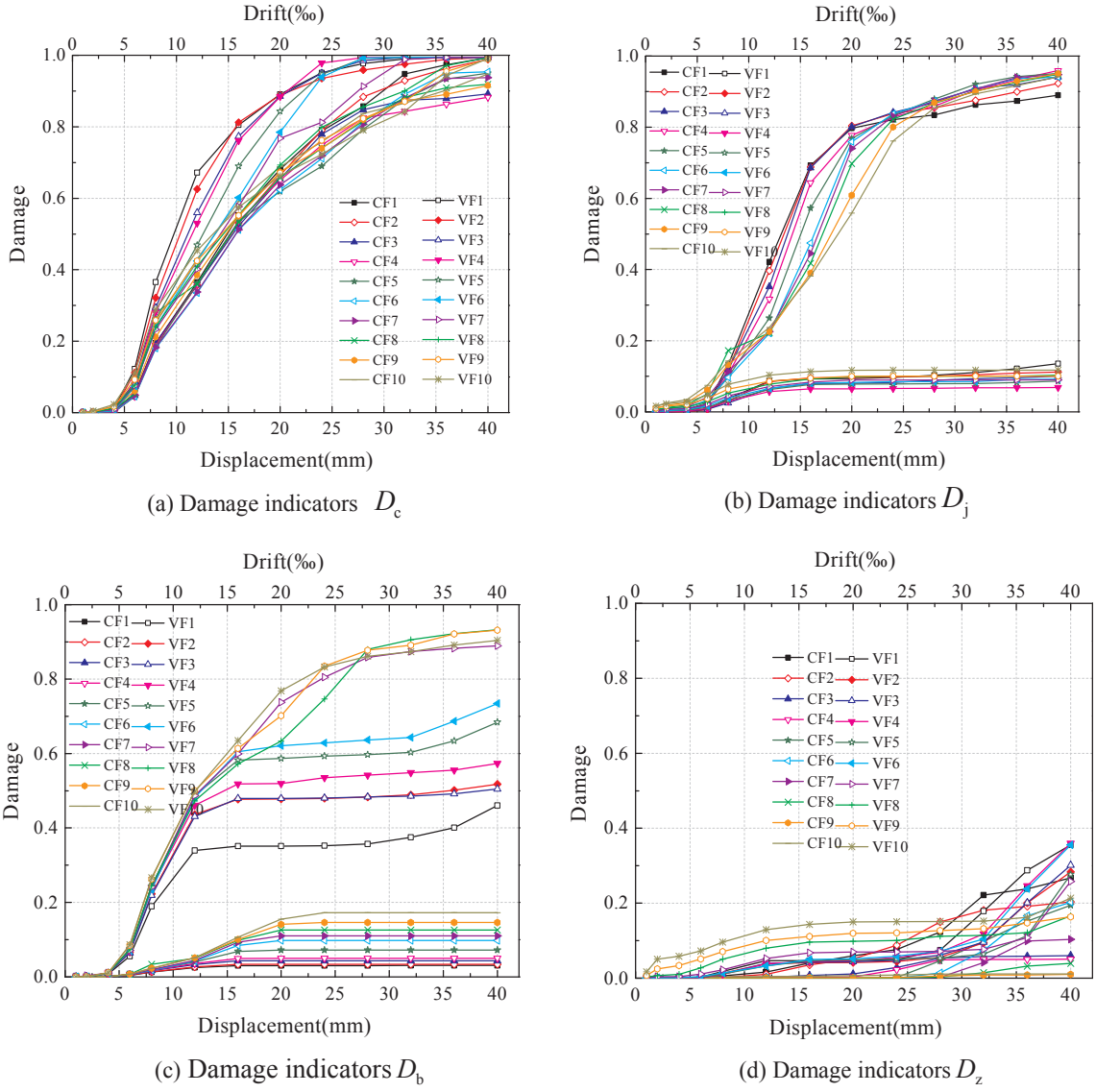

Fig. 18. Four damage indicators with the change of loading displacement amplitude.

4.3. Comparative analysis of damage evolution

Fig. 18 illustrates four damage indicators of D_c, D_j, D_b and D_z with the change of loading displacement amplitude under each level of ALR.

From the overall view of Fig. 18(a), the damage indicator D_c of the frame structure increases gradually with the increase of loading displacement amplitude. Under the small displacement amplitude of 0–6 mm, the damage indicator D_c of the frame structure presents the small values and grows slowly. And it is insensitive to the change of ALR. Under the medium displacement amplitude of 6–24 mm, the damage indicator D_c of VFs is larger than that of CFs and the growth rate of D_c for VFs is greater than that for CFs with the increase of loading displacement amplitude at the same ALR. At the same loading displacement amplitude, the damage indicator D_c of VFs decreases gradually and the damage indicator D_c of CFs is not significantly changed with the increase of ALR. Under the large displacement amplitude of 24–40 mm, the growth rate of damage indicator D_c decreases gradually and the value of damage indicator D_c gradually increases to approach 1 with the increase of loading displacement amplitude. It indicates that the damage at the column bottom is magnified after the HVEDB is added to the frame structure. Under the medium displacement amplitude of 6–24 mm, the damage indicator D_c is sensitive to change of ALR, and the amplification effect on the damage of column bottom is weakened with the increase of ALR. Further the rationality of selecting damage indicator D_c is verified.

From the overall view of Fig. 18(b), the damage at the beam-column joints of VFs is much smaller than that of CFs during the whole loading process. Under the small displacement amplitude of 0–6 mm, the damage indicator D_j of the frame structure presents the small values and grows slowly. And it is insensitive to the change of ALR. Under the medium displacement amplitude of 6–24 mm, the damage indicator D_j of CFs rises quickly with the increase of loading displacement amplitude. At the same loading displacement amplitude, the damage indicator D_j decreases gradually with the increase of ALR. The damage indicator D_j of VFs rises very slowly, and the value of damage indicator D_j is less than 0.11. The damage indicator D_j is insensitive to change of ALR. Under the large displacement amplitude of 24–40 mm, the growth rate of damage indicator D_j for CFs decreases gradually as the loading displacement amplitude increases, and the sensitivity of damage indicator D_j to the change of ALR gradually reduces. The value of damage indicator D_j for CFs gradually increases to approach 1. The growth rate of damage indicator D_j for VFs approaches zero, and the value of damage indicator D_j is less than 0.15. The damage indicator D_j is insensitive to change of ALR. It indicates that the damage development at

the beam-column joints is well inhibited by the addition of HVEDB to the frame structure. Further the rationality of selecting damage indicator D_j is verified.

As can be seen from Fig. 18(c), under the small displacement amplitude of 0–6 mm, the damage indicator D_b of the frame structure presents the small values and grows slowly. And it is insensitive to the change of ALR. Under the medium displacement amplitude of 6–24 mm, the damage indicator D_b of VFs rises rapidly and the damage indicator D_b of CFs increases slowly with the increase of loading displacement amplitude. The damage indicator D_b of VFs is much larger than that of CFs at the same ALR. At the same loading displacement amplitude, the damage indicator D_b of VFs and CFs both increases gradually with the increase of ALR, and the change amplitude about the damage indicator D_b for VFs is greater than that for CFs. Under the large displacement amplitude of 24–40 mm, the growth of the damage indicator D_b for CFs tends to stop and the growth rate of the damage indicator D_b for VFs decreases gradually with the increase of loading displacement amplitude. At the same loading displacement amplitude, the damage indicator D_b of VFs and CFs both increases gradually with the increase of ALR, and the change amplitude about the damage indicator D_b for VFs is greater than that for CFs. The maximum value of the damage index D_b for VFs approaches 1 at the large ALR of 0.7–1.0. It indicates that the damage of the frame beam where the HVEDB is added is more serious, and the damage degree increases gradually with the increase of ALR. The above-mentioned locations should be especially enhanced in the seismic design of the structure. Further the rationality of selecting damage indicator D_b is verified.

As can be seen from Fig. 18(d), under the small and medium displacement amplitude of 0–24 mm, the damage indicator D_z of VFs is larger than that of CFs at the same loading displacement amplitude and ALR. At the same loading displacement amplitude, the damage indicator D_z of CFs changes little and the damage indicator D_z of VFs grows slowly with the increase of ALR. Under the large displacement amplitude of 24–40 mm, the damage indicator D_z of VFs still remains so small, and the maximum value of damage indicator D_z under various working conditions is less than 0.36. It indicates that the damage of the frame column where the HVEDB is added for VFs is so small, and it is not the bottleneck for the seismic design of VF.

5. Summary and conclusions

In this study, the seismic behavior of ten CFs and ten VFs are conducted under horizontal sinusoidal steady-state excitation. On this basis, a comparative study on the damage evolution about two types of frames at the material scale in the whole process is carried out. The following main conclusions can be obtained.

(1) For the cases considered in this study, the addition of HVEDB can greatly improve the load-bearing capacity (about 50% increase), lateral stiffness (more than 40% increase) and energy dissipation capacity (more than 2.4 times increase under low ALR and increased by up to 7.15 times under high ALR) of the frame structure. The HVEDB produces a significant inhibition effect on the load-bearing capacity degradation and stiffness degradation of the structure, and this restriction effect can be enhanced as the ALR increases.
(2) When the ALR is in the range of 0.1–1.0, the energy dissipation capacity of VFs slightly reduces first and then gradually rises with the increase of ALR. And the energy dissipation capacity of VFs reaches a minimum under the ALR of 0.4. When the ALR is in the range of 0.1–0.6, the average additional damping ratio and energy dissipation capability of VFs remain basically stable, and the energy dissipation of HVEDB increases slowly with the increase of displacement amplitude. When the ALR is in the range of 0.6–1.0, the average additional damping ratio and energy dissipation capability of VFs gradually increase with the increase of ALR, and the energy dissipation of HVEDB increases rapidly with the increase of displacement amplitude.
(3) The force mode and failure mode of the frames are changed by the addition of HVEDB. The rebar strain at the beam-column joints of VFs significantly reduces. The HVEDB can provide the effective protection for the beam-column joints by transferring the damage region from the beam-column joint to the frame beam successfully, which guarantees the seismic design requirements of “strong nodes and weak components” avoiding the brittle failure mode of RC frames under high ALR. The compressive damage of VFs is concentrated at the 0–1/3H of the column bottom and the beam with HVEDB. The above-mention locations where the compressive damage is concentrated at should be especially enhanced in the seismic design of the structure.

In summary, the retrofitted RC frame structures by adding haunch viscoelastic damping braces is a novel and advanced structural system. It is worthy of further development, especially for the RC frame structures with insufficient seismic design and the local weak locations of the frame column designed under high ALR.

Acknowledgements

Financial supports for this research are provided by National Science Fund for Distinguished Young Scholars (51625803), Program of Chang Jiang Scholars of Ministry of Education, Ten Thousand Talent Program of Leading Technologists, The National Key Research and Development Program of China (2016YFE0200500 and 2016YFE0119700), Postgraduate Research & Practice Innovation Program of Jiangsu Province (KYCX18_0112). These supports are acknowledged gratefully.

References

[1] Burton H, Deierlein G. Simulation of seismic collapse in nonductile reinforced concrete frame buildings with masonry infills. J Struct Eng 2013;140(8):A4014016.
[2] Liel AB, Haselton CB, Deierlein GG. Seismic collapse safety of reinforced concrete buildings. II: Comparative assessment of nonductile and ductile moment frames. J Struct Eng 2010;137(4):492–502.
[3] Zhao B, Taucer F, Rossetto T. Field investigation on the performance of building structures during the 12 May 2008 Wenchuan earthquake in China. Eng Struct 2009;31(8):1707–23.
[4] Westenenk B, de la Llera JC, Jünemann R, et al. Analysis and interpretation of the seismic response of RC buildings in Concepción during the February 27, 2010, Chile earthquake. B Earthq Eng 2013;11(1):69–91.
[5] Cheng Y, Bai G, Dong Y. Spectrum characterization of two types of long-period ground motions and seismic behavior of frame-core wall structures under multi-dimensional earthquake records. Struct Des Tall Spec 2018;27(16). e1539.
[6] Park R. A summary of results of simulated seismic load tests on reinforced concrete beam-column joints, beams and columns with substandard reinforcing details. J Earthq Spectra 2002;6(02):147–74.
[7] Li B, Wu Y, Pan TC. Seismic behaviour of non-seismically detailed interior beam-wide column joints; part I: experimental results and observed behavior. ACI Struct J 2002;99(6):791–802.
[8] Karayannis CG, Chalioris CE, Sirkelis GM. Local retrofit of exterior RC beam–column joints using thin RC jackets—An experimental study. Earthq Eng Struct D 2008;37(5):727–46.
[9] Li B, Lam ES, Wu B, et al. Experimental investigation on reinforced concrete interior beam–column joints rehabilitated by ferrocement jackets. Eng Struct 2013;56:897–909.
[10] De Matteis G, Formisano A, Mazzolani FM. An innovative methodology for seismic retrofitting of existing RC buildings by metal shear panels. Earthq Eng Struct D 2009;38(1):61–78.
[11] Yen JYR, Chien HK. Steel plates rehabilitated RC beam–column joints subjected to vertical cyclic loads. Constr Build Mater 2010;24(3):332–9.
[12] Sharbatdar MK, Kheyroddin A, Emami E. Cyclic performance of retrofitted reinforced concrete beam–column joints using steel prop. Constr Build Mater 2012;36:287–94.
[13] Pampanin S, Christopoulos C, Chen TH. Development and validation of a metallic haunch seismic retrofit solution for existing under-designed RC frame buildings. Earthq Eng Struct D 2006;35(14):1739–66.
[14] Mahrenholtz C, Lin PC, Wu AC, et al. Retrofit of reinforced concrete frames with buckling-restrained braces. Earthq Eng Struct D 2015;44(1):59–78.
[15] Guerrero H, Ji T, Teran-Gilmore A, et al. A method for preliminary seismic design and assessment of low-rise structures protected with Buckling-Restrained Braces.

Eng Struct 2016;123:141–54.
[16] Sasmal S, Nath D. Seismic performance of non-invasive single brace made of steel and shape memory alloy for retrofit of gravity load designed sub-assemblages. Eng Struct 2017;143:316–29.
[17] Mazza F. Shear modelling of the beam-column joint in the nonlinear static analysis of rc framed structures retrofitted with damped braces. B Earthq Eng 2018;16(5):2043–66.
[18] Di Ludovico M, Prota A, Manfredi G, et al. Seismic strengthening of an under-designed RC structure with FRP. Earthq Eng Struct D 2008;37(1):141–62.
[19] Esmaeeli E, Barros JAO, Sena-Cruz J, et al. Retrofitting of interior RC beam–column joints using CFRP strengthened SHCC: cast-in-place solution. Compos Struct 2015;122:456–67.
[20] Sasmal S, Khatri CP, Karusala R. Numerical simulation of performance of near-surface mounted FRP-upgraded beam–column sub-assemblages under cyclic loading. Struct Infrastruct E 2015;11(8):1012–27.
[21] Mostofinejad D, Hosseini SM, Tehrani BN, et al. Innovative warp and woof strap (WWS) method to anchor the FRP sheets in strengthened concrete beams. Constr Build Mater 2019;218:351–64.
[22] Sasmal S, Novák B, Ramanjaneyulu K. Numerical analysis of fiber composite-steel plate upgraded beam–column sub-assemblages under cyclic loading. Compos Struct 2011;93(2):599–610.
[23] Le-Trung K, Lee K, Lee J, et al. Experimental study of RC beam–column joints strengthened using CFRP composites. Compos Part B-Eng 2010;41(1):76–85.
[24] Singh V, Bansal PP, Kumar M, et al. Experimental studies on strength and ductility of CFRP jacketed reinforced concrete beam-column joints. Constr Build Mater 2014;55:194–201.
[25] Hsieh CT, Lin Y. Detecting debonding flaws at the epoxy–concrete interfaces in near-surface mounted CFRP strengthening beams using the impact–echo method. Ndt & E Int 2016;83:1–13.
[26] Jiang SF, Zeng X, Shen S, et al. Experimental studies on the seismic behavior of earthquake-damaged circular bridge columns repaired by using combination of near-surface-mounted BFRP bars with external BFRP sheets jacketing. Eng Struct 2016;106:317–31.
[27] Bedirhanoglu I, Ilki A, Kumbasar N. Precast fiber reinforced cementitious composites for seismic retrofit of deficient RC joints–a pilot study. Eng Struct 2013;52:192–206.
[28] Röhm C, Novák B, Sasmal S, et al. Behaviour of fibre reinforced beam-column sub-assemblages under reversed cyclic loading. Constr Build Mater 2012;36:319–29.
[29] Xu ZD, Shen YP, Zhao HT. A synthetic optimization analysis method on structures with viscoelastic dampers. Soil Dyn Earthq Eng 2003;23(8):683–9.
[30] Xu ZD. Earthquake mitigation study on viscoelastic dampers for reinforced concrete structures. J Vib Control 2007;13(1):29–43.
[31] Xu ZD, Liao YX, Ge T, et al. Experimental and theoretical study of viscoelastic dampers with different matrix rubbers. J Eng Mech 2016;142(8):04016051.
[32] Xu ZD, Zhao HT, Li AQ. Optimal analysis and experimental study on structures with viscoelastic dampers. J Sound Vib. 2004;273(3):607–18.
[33] Hibbitt HD, Karlsson BI, Sorensen EP. ABAQUS user's manual. Providence(RI): Dassault Systemes Simulia Corp; 2011.
[34] (GB50010–2010) Code for design of concrete structures [in Chinese].
[35] Dong YR, Xu ZD, Zeng K, et al. Seismic behavior and cross-scale refinement model of damage evolution for RC shear walls. Eng Struct 2018;167:13–25.
[36] Xu ZD, Xu C, Hu J. Equivalent fractional Kelvin model and experimental study on viscoelastic damper. J Vib Control 2015;21(13):2536–52.
[37] Zhou Y, Yin QL, Lin SM. Experimental investigation on seismic performance of RC frame structures with viscous damper energy dissipation haunch braces. J Build Struct 2011;32(11):64–73. [in Chinese].
[38] Sezen H, Moehle JP. Seismic tests of concrete columns with light transverse reinforcement. ACI Struct J 2006;103(6):842.
[39] Xiao J, Zhang C. Seismic behavior of RC columns with circular, square and diamond sections. Constr Build Mater 2008;22(5):801–10.
[40] Park YJ, Ang AHS. Mechanistic seismic damage model for reinforced concrete. J Struct Eng 1985;111(4):722–39.